

Dynamical Hartree-Fock-Bogoliubov Theory of Vortices in Bose-Einstein Condensates at Finite Temperature

B. G. Wild and D. A. W. Hutchinson

*The Jack Dodd Centre for Quantum Technology, Department of Physics,
University of Otago, Dunedin 9054, New Zealand*

We present a method utilizing the continuity equation for the condensate density to make predictions of the precessional frequency of single off-axis vortices and of vortex arrays in Bose-Einstein condensates at finite temperature. We also present an orthogonalized Hartree-Fock-Bogoliubov (HFB) formalism. We solve the continuity equation for the condensate density self-consistently with the orthogonalized HFB equations, and find stationary solutions in the frame rotating at this frequency. As an example of the utility of this formalism we obtain time-independent solutions for quasi-two-dimensional rotating systems in the co-rotating frame. We compare these results with time-dependent predictions where we simulate stirring of the condensate.

Keywords:

I. INTRODUCTION

One of the characteristics of a superfluid is the quantization of vortices that are found when sufficient angular momentum is present in the system. Vortices, as a signature of superfluidity, are therefore of great theoretical and experimental interest, and the reader is referred to the recent review article by Fetter [1]. Our model is based on the Hartree-Fock-Bogoliubov (HFB) formalism [2–5]. We demonstrate how the continuity equation for the condensate density, solved self-consistently with a set of time-independent orthogonalized Hartree-Fock-Bogoliubov (HFB) equations in the frame rotating at the precessional frequency, can be used to make *a priori* predictions of the precessional frequencies of vortices in Bose-Einstein condensates (BECs). By introducing a set of modified basis functions incorporating the vortex positions one is able to do this not only for single off-axis vortices, but also for the multiple vortex case. In order to perform these calculations correctly, it is necessary that the condensate and thermal populations be mutually orthogonal. We present an orthogonal HFB formalism in which this condition holds, and for which we show the existence of a zero-energy eigenvalue in the time-independent case, in contrast with the standard HFB formalism. As an illustration we model a two-dimensional BEC system, establishing the dependency of the precessional frequency Ω on the lattice parameter a and on the temperature T for triangular and hexagonal vortex arrays. We also show the relationship of Ω with T for the case of two vortices and for triangular and hexagonal vortex arrays with three and seven vortices, respectively, having lattice parameter $a = 3$ harmonic oscillator units, establishing the existence of an upper bound for the precessional frequency as a function of the number of vortices. We obtain qualitative agreement with the areal density approximation [6, 7] (see also Ref. [8]) for the hexagonal vortex array. We verify the validity of these predictions in a series of finite temperature simulations using time-dependent HFB [9, 10]. We use one or more Gaussian stirrers to impart angular momentum

to the BEC, and establish a critical stirring frequency required for the creation of vortices corresponding to a local stirring velocity just in excess of the local Landau critical velocity. We also verify that the axial component of the angular momentum is conserved when the trapping potential is axially symmetric, thus satisfying Noether's theorem. We show that angular momentum is lost when this symmetry is broken, leading to the decay of vortices.

II. FORMALISM

We consider a BEC system in the frame rotating with angular frequency Ω with grand-canonical Bose Hamiltonian given by

$$\hat{H}^{(GC)}(t) = \int d\mathbf{r} \left[\hat{\psi}^\dagger(\mathbf{r}, t) \left(\hat{h}_\Omega(\mathbf{r}) - \mu \right) \hat{\psi}(\mathbf{r}, t) + \frac{g}{2} \hat{\psi}^\dagger(\mathbf{r}, t) \hat{\psi}^\dagger(\mathbf{r}, t) \hat{\psi}(\mathbf{r}, t) \hat{\psi}(\mathbf{r}, t) \right]. \quad (1)$$

where $\hat{h}_\Omega(\mathbf{r})$ is the single-particle Hamiltonian

$$\hat{h}_\Omega(\mathbf{r}) = -\frac{\hbar^2}{2m} \nabla^2 + i\hbar\Omega \cdot (\mathbf{r} \times \nabla) + V_T(\mathbf{r}), \quad (2)$$

and

$$g = \frac{4\pi\hbar^2 a_s}{m}, \quad (3)$$

with a_s the s -wave scattering length. We wish to obtain an HFB formalism such that the condensate and thermal modes are orthogonal. We proceed by splitting the Bose field operator $\hat{\psi}(\mathbf{r}, t)$ into a coherent part represented by the condensate field operator $\hat{\Phi}(\mathbf{r}, t)$, and an incoherent part represented by the fluctuation operator $\hat{\eta}(\mathbf{r}, t)$, writing $\hat{\psi}(\mathbf{r}, t) = \hat{\Phi}(\mathbf{r}, t) + \hat{\eta}(\mathbf{r}, t)$ with $\hat{\Phi}(\mathbf{r}, t) \equiv \phi(\mathbf{r}, t) \hat{a}_c(t)$, with $\hat{a}_c(t)$ the annihilation operator for the condensate, and $\phi(\mathbf{r}, t)$ a condensate wave function satisfying the normalization condition $\int d\mathbf{r} |\phi(\mathbf{r}, t)|^2 = 1$. The fluctuation operator $\hat{\eta}(\mathbf{r}, t)$ is defined as [11] $\hat{\eta}(\mathbf{r}, t) \equiv$

$\hat{\psi}(\mathbf{r}, t) - \phi(\mathbf{r}, t) \int d\mathbf{r}' \phi^*(\mathbf{r}', t) \hat{\psi}(\mathbf{r}', t)$. It can then be shown that the orthogonality condition

$$\int d\mathbf{r} \phi^*(\mathbf{r}, t) \hat{\eta}(\mathbf{r}, t) = 0 \quad (4)$$

holds, so the condensate and thermal populations are orthogonal, as required. We also find from the definition of $\hat{\eta}$ that $\hat{a}_c(t) = \int d\mathbf{r} \phi^*(\mathbf{r}, t) \hat{\psi}(\mathbf{r}, t)$. In addition $\hat{\Phi}$ and $\hat{\eta}$ satisfy the commutation relations

$$\begin{cases} [\hat{\Phi}(\mathbf{r}, t), \hat{\psi}^\dagger(\mathbf{r}', t)] = \phi(\mathbf{r}, t) \phi^*(\mathbf{r}', t), \\ [\hat{\Phi}(\mathbf{r}, t), \hat{\psi}(\mathbf{r}', t)] = [\hat{\Phi}^\dagger(\mathbf{r}, t), \hat{\psi}^\dagger(\mathbf{r}', t)] = 0 \end{cases} \quad (5)$$

and

$$\begin{cases} [\hat{\eta}(\mathbf{r}, t), \hat{\psi}^\dagger(\mathbf{r}', t)] = \delta(\mathbf{r} - \mathbf{r}') - \phi(\mathbf{r}, t) \phi^*(\mathbf{r}', t) \equiv Q(\mathbf{r}, \mathbf{r}', t), \\ [\hat{\eta}(\mathbf{r}, t), \hat{\psi}(\mathbf{r}', t)] = [\hat{\eta}^\dagger(\mathbf{r}, t), \hat{\psi}^\dagger(\mathbf{r}', t)] = 0 \end{cases} \quad (6)$$

respectively. We use the Bogoliubov transformation

$$\hat{\eta}(\mathbf{r}, t) = \sum_k \left(u_k(\mathbf{r}, t) \hat{a}_k + v_k^*(\mathbf{r}, t) \hat{a}_k^\dagger \right) \quad (7)$$

to diagonalize the grand-canonical Hamiltonian (as with standard HFB), where we assume that the operators \hat{a}_k obey the Bosonic commutation relations

$$[\hat{a}_k, \hat{a}_l^\dagger] = \delta_{kl} \quad \text{and} \quad [\hat{a}_k, \hat{a}_l] = [\hat{a}_k^\dagger, \hat{a}_l^\dagger] = 0. \quad (8)$$

We use the respective Heisenberg equations of motion for the operators $\hat{\Phi}$ and $\hat{\eta}$ and the commutation relations

$$\begin{cases} [\hat{\psi}(\mathbf{r}, t), \hat{a}_q^\dagger] = u_q(\mathbf{r}, t), & [\hat{a}_q, \hat{\psi}(\mathbf{r}, t)] = v_q^*(\mathbf{r}, t), \\ [\hat{\psi}^\dagger(\mathbf{r}, t), \hat{a}_q^\dagger] = v_q(\mathbf{r}, t), & [\hat{a}_q, \hat{\psi}^\dagger(\mathbf{r}, t)] = u_q^*(\mathbf{r}, t) \end{cases} \quad (9)$$

for the quasi-particle annihilation and creation operators \hat{a}_q and \hat{a}_q^\dagger to derive the equations

$$\int d\mathbf{r}' \phi^* \left[-i\hbar \frac{\partial \hat{\Phi}}{\partial t} + (\hat{h}_\Omega - \mu + g\hat{\psi}^\dagger \hat{\psi}) \hat{\psi} \right] = 0 \quad (10)$$

for the condensate operator $\hat{\Phi}$, and

$$i\hbar \frac{\partial u_q(\mathbf{r}, t)}{\partial t} = \int d\mathbf{r}' \left[\hat{L}(\mathbf{r}, \mathbf{r}', t) u_q(\mathbf{r}', t) + \hat{M}(\mathbf{r}, \mathbf{r}', t) v_q(\mathbf{r}', t) \right] \quad (11)$$

and

$$i\hbar \frac{\partial v_q^*(\mathbf{r}, t)}{\partial t} = \int d\mathbf{r}' \left[\hat{L}(\mathbf{r}, \mathbf{r}', t) v_q^*(\mathbf{r}', t) + \hat{M}(\mathbf{r}, \mathbf{r}', t) u_q^*(\mathbf{r}', t) \right] \quad (12)$$

for the quasi-particle amplitudes u_q and v_q , where we have defined the operators

$$\begin{aligned} \hat{L}(\mathbf{r}, \mathbf{r}', t) &\equiv Q(\mathbf{r}, \mathbf{r}', t) \left(\hat{h}(\mathbf{r}') - \mu + 2g\hat{\psi}^\dagger(\mathbf{r}', t) \hat{\psi}(\mathbf{r}', t) \right) \\ \hat{M}(\mathbf{r}, \mathbf{r}', t) &\equiv Q(\mathbf{r}, \mathbf{r}', t) \left(g\hat{\psi}(\mathbf{r}', t) \hat{\psi}^\dagger(\mathbf{r}', t) \right) \end{aligned} \quad (13)$$

for notational convenience. We note that the quantity in square brackets in Eq. (10) is orthogonal to ϕ^* . Hence we can re-write (10) in the form

$$i\hbar \frac{\partial \hat{\Phi}(\mathbf{r}, t)}{\partial t} = \left(\hat{h}_\Omega - \mu + g\hat{\psi}^\dagger(\mathbf{r}, t) \hat{\psi}(\mathbf{r}, t) \right) \hat{\psi}(\mathbf{r}, t) - \hat{A}(\mathbf{r}, t) \quad (14)$$

where $\hat{A}(\mathbf{r}, t)$ is a quantity orthogonal to ϕ , i.e. $\int d\mathbf{r} \phi^* \hat{A}(\mathbf{r}, t) = 0$ chosen such that angular and linear momentum conservation hold. Using the mean-field approximations $\hat{a}_c \phi \rightarrow \Phi$, $\hat{\eta}^\dagger \hat{\eta} \rightarrow \langle \hat{\eta}^\dagger \hat{\eta} \rangle \equiv \tilde{n}$, $\hat{\eta} \hat{\eta} \rightarrow \langle \hat{\eta} \hat{\eta} \rangle \equiv \tilde{m}$, $\hat{\eta}^\dagger \hat{\eta}^\dagger \rightarrow \langle \hat{\eta}^\dagger \hat{\eta}^\dagger \rangle \equiv \tilde{m}^*$, and $\hat{\psi}^\dagger \hat{\psi} \hat{\psi} \rightarrow \langle \hat{\psi}^\dagger \hat{\psi} \hat{\psi} \rangle = (|\Phi|^2 + 2\tilde{n}) \Phi + \tilde{m} \Phi^*$ and result (25) for \hat{A} which we prove shortly, we then obtain the orthogonal HFB equations consisting of the modified generalized Gross-Pitaevskii equation (GGPE)

$$\begin{aligned} i\hbar \frac{\partial \Phi(\mathbf{r}, t)}{\partial t} &= \left(\hat{h}(\mathbf{r}) - \mu + g \left(|\Phi|^2 + 2\tilde{n} \right) \right) \Phi(\mathbf{r}, t) \\ &\quad + g\tilde{m} \Phi^*(\mathbf{r}, t) - \int d\mathbf{r}' \hat{P}(\mathbf{r}', \mathbf{r}, t) \phi(\mathbf{r}', t) \end{aligned} \quad (15)$$

and the orthogonal Bogoliubov-de Gennes equations (BdGEs)

$$i\hbar \frac{\partial}{\partial t} \mathbf{w}_q(\mathbf{r}, t) = \int d\mathbf{r}' \hat{\mathbf{L}}(\mathbf{r}, \mathbf{r}', t) \mathbf{w}_q(\mathbf{r}', t) \quad (16)$$

where we have defined the matrix operator

$$\hat{\mathbf{L}}(\mathbf{r}, \mathbf{r}', t) \equiv \begin{bmatrix} \hat{\mathcal{L}}(\mathbf{r}, \mathbf{r}', t) & \hat{\mathcal{M}}(\mathbf{r}, \mathbf{r}', t) \\ -\hat{\mathcal{M}}^*(\mathbf{r}, \mathbf{r}', t) & -\hat{\mathcal{L}}^*(\mathbf{r}, \mathbf{r}', t) \end{bmatrix} \quad (17)$$

and the vector

$$\mathbf{w}_q(\mathbf{r}, t) \equiv \begin{bmatrix} u_q(\mathbf{r}, t) \\ v_q(\mathbf{r}, t) \end{bmatrix} \quad (18)$$

for the quasi-particle amplitudes. The operators $\hat{P}(\mathbf{r}', \mathbf{r}, t)$, $\hat{\mathcal{L}}(\mathbf{r}, \mathbf{r}', t)$ and $\hat{\mathcal{M}}(\mathbf{r}, \mathbf{r}', t)$ are defined by

$$\hat{P}(\mathbf{r}', \mathbf{r}, t) \equiv \frac{\left(\tilde{n}(\mathbf{r}', \mathbf{r}, t) \hat{\mathcal{L}}(\mathbf{r}', t) + \tilde{m}(\mathbf{r}', \mathbf{r}, t) \hat{\mathcal{M}}^*(\mathbf{r}', t) \right)}{\sqrt{N_c(t)}} \quad (19)$$

and

$$\begin{aligned} \hat{\mathcal{L}}(\mathbf{r}, \mathbf{r}', t) &\equiv Q(\mathbf{r}, \mathbf{r}', t) \hat{\mathcal{L}}(\mathbf{r}', t), \\ \hat{\mathcal{M}}(\mathbf{r}, \mathbf{r}', t) &\equiv Q(\mathbf{r}, \mathbf{r}', t) \hat{\mathcal{M}}(\mathbf{r}', t) \end{aligned} \quad (20)$$

where

$$\begin{aligned} \hat{\mathcal{L}}(\mathbf{r}, t) &\equiv \hat{h}_\Omega(\mathbf{r}) - \mu + 2g \left(|\Phi(\mathbf{r}, t)|^2 + \tilde{n}(\mathbf{r}, t) \right) \\ \hat{\mathcal{M}}(\mathbf{r}, t) &\equiv g \left(\Phi^2(\mathbf{r}, t) + \tilde{m}(\mathbf{r}, t) \right), \end{aligned} \quad (21)$$

with the definitions

$$\begin{aligned} \tilde{n}(\mathbf{r}', \mathbf{r}, t) &\equiv \langle \hat{\eta}^\dagger(\mathbf{r}', t) \hat{\eta}(\mathbf{r}, t) \rangle \\ &= \sum_q \left[u_q^*(\mathbf{r}', t) u_q(\mathbf{r}, t) N_{BE}(\epsilon_q) \right. \\ &\quad \left. + v_q(\mathbf{r}', t) v_q^*(\mathbf{r}, t) (N_{BE}(\epsilon_q) + 1) \right] \end{aligned} \quad (22)$$

and

$$\begin{aligned}\tilde{m}(\mathbf{r}', \mathbf{r}, t) &\equiv \langle \hat{\eta}(\mathbf{r}', t) \hat{\eta}(\mathbf{r}, t) \rangle \\ &= \sum_q [v_q^*(\mathbf{r}', t) u_q(\mathbf{r}, t) N_{BE}(\epsilon_q) \\ &\quad + u_q(\mathbf{r}', t) v_q^*(\mathbf{r}, t) (N_{BE}(\epsilon_q) + 1)]\end{aligned}\quad (23)$$

for the normal and anomalous correlation functions $\tilde{n}(\mathbf{r}', \mathbf{r}, t)$ and $\tilde{m}(\mathbf{r}', \mathbf{r}, t)$, where

$$N_{BE}(\epsilon_q) = \frac{1}{\exp(\beta\epsilon_q) - 1} \quad (24)$$

is the usual Bose distribution, with $\beta \equiv 1/k_B T$ the temperature parameter, and k_B is the Boltzmann constant. Clearly $\tilde{n}(\mathbf{r}, t) \equiv \tilde{n}(\mathbf{r}, \mathbf{r}, t)$ and $\tilde{m}(\mathbf{r}, t) \equiv \tilde{m}(\mathbf{r}, \mathbf{r}, t)$ represent the usual thermal and anomalous densities. To prove Eq. (15), we note using results from vector calculus, that we can write [12]

$$\begin{aligned}\frac{d}{dt} \langle \hat{\mathbf{L}} \rangle &= \frac{d}{dt} \langle \int d\mathbf{r} \hat{\psi}^\dagger(\mathbf{r}, t) \hat{\mathbf{L}} \hat{\psi}(\mathbf{r}, t) \rangle \\ &= \frac{1}{i\hbar} \int d\mathbf{r} \left\{ |\Phi|^2 \hat{\mathbf{L}} V_T + |\Phi|^2 \hat{\mathbf{L}} (|\Phi|^2 + 2\tilde{n}) \right. \\ &\quad + \tilde{n} \hat{\mathbf{L}} V_T + 2\tilde{n} \hat{\mathbf{L}} (|\Phi|^2 + \tilde{n}) \\ &\quad - \frac{1}{2} g \tilde{m}^* \hat{\mathbf{L}} (\Phi^2) - \frac{1}{2} g \tilde{m} \hat{\mathbf{L}} (\Phi^{*2}) \\ &\quad - \frac{1}{2} g (\Phi^{*2} + \tilde{m}^*) \hat{\mathbf{L}} \tilde{m} - \frac{1}{2} g (\Phi^2 + \tilde{m}) \hat{\mathbf{L}} \tilde{m}^* \\ &\quad + \left\langle -\hat{A}^\dagger + \frac{1}{\sqrt{N_c}} \hat{\eta}^\dagger(\mathbf{r}, t) \int d\mathbf{r}' \hat{\eta}(\mathbf{r}', t) \hat{\mathcal{L}}^*(\mathbf{r}', t) \phi^*(\mathbf{r}', t) \right. \\ &\quad + \left. \frac{1}{\sqrt{N_c}} \hat{\eta}^\dagger(\mathbf{r}, t) \int d\mathbf{r}' \hat{\eta}^\dagger(\mathbf{r}', t) \hat{\mathcal{M}}(\mathbf{r}', t) \phi^*(\mathbf{r}', t) \right\rangle \hat{\mathbf{L}} \Phi \\ &\quad + \left\langle -\hat{A} + \frac{1}{\sqrt{N_c}} \left(\int d\mathbf{r}' \hat{\eta}^\dagger(\mathbf{r}', t) \hat{\mathcal{L}}(\mathbf{r}', t) \phi(\mathbf{r}', t) \right) \hat{\eta}(\mathbf{r}, t) \right. \\ &\quad + \left. \frac{1}{\sqrt{N_c}} \left(\int d\mathbf{r}' \hat{\eta}(\mathbf{r}', t) \hat{\mathcal{M}}^*(\mathbf{r}', t) \phi(\mathbf{r}', t) \right) \hat{\eta}(\mathbf{r}, t) \right\rangle \hat{\mathbf{L}} \Phi^* \Big\} \\ &= \frac{1}{i\hbar} \int d\mathbf{r} (|\Phi|^2 + \tilde{n}) \hat{\mathbf{L}} V_T.\end{aligned}$$

provided we choose

$$\hat{A} = \frac{\int d\mathbf{r}' \left(\hat{\eta}^\dagger(\mathbf{r}', t) \hat{\mathcal{L}}(\mathbf{r}', t) + \hat{\eta}(\mathbf{r}', t) \hat{\mathcal{M}}^*(\mathbf{r}', t) \right) \phi(\mathbf{r}', t) \hat{\eta}(\mathbf{r}, t)}{\sqrt{N_c(t)}}, \quad \frac{\partial}{\partial t} |\Phi(\mathbf{r}, t)|^2 + \nabla \cdot \mathbf{j}(\mathbf{r}, t) = \Omega \cdot (\mathbf{r} \times \nabla) |\Phi(\mathbf{r}, t)|^2 - \frac{i}{\hbar} C(\mathbf{r}, t) \quad (28)$$

thus ensuring that angular and linear momentum are conserved. Since standard HFB is a ϕ -derivable, and hence a conserving, theory, particle number and both angular and linear momentum conservation hold for standard HFB. It can be shown that particle number, and both angular and linear momentum conservation also hold for this formalism, the latter being ensured by the inclusion of the operator \hat{P} in (15). The corresponding time-independent equations are given by the modified GGPE

$$\begin{aligned}\mu \Phi(\mathbf{r}) &= \left(\hat{h}_\Omega(\mathbf{r}) + g (|\Phi|^2 + 2\tilde{n}) \right) \Phi(\mathbf{r}) \\ &\quad + g \tilde{m} \Phi^*(\mathbf{r}) - \int d\mathbf{r}' \hat{P}(\mathbf{r}', \mathbf{r}) \phi(\mathbf{r}')\end{aligned}\quad (26)$$

and the orthogonal BdGEs

$$\epsilon_q \mathbf{w}_q(\mathbf{r}) = \int d\mathbf{r}' \hat{\mathbf{L}}(\mathbf{r}, \mathbf{r}') \mathbf{w}_q(\mathbf{r}') \quad (27)$$

where the operators $\hat{\mathbf{L}}$ and \hat{P} are now time independent. To show the existence of a null subspace of zero-energy

eigenvalue modes for the orthogonal BdGEs (27) spanned by the mode $(\phi, -\phi^*)$, let us write $u_0(\mathbf{r}) = \alpha \phi(\mathbf{r})$, $v_0(\mathbf{r}) = -\beta \phi^*(\mathbf{r})$ for some $\alpha, \beta \in \mathbb{C}$, where $\phi(\mathbf{r}) = \Phi(\mathbf{r})/\sqrt{N_c}$, and $\phi(\mathbf{r})$ is normalized to unity, i.e.,

$$\int d\mathbf{r} |\phi(\mathbf{r})|^2 = 1.$$

Then, substituting u_0, v_0 into the first of the modified time-independent BdGEs (27), we find that

$$\begin{aligned}\epsilon_0 \phi &= \int d\mathbf{r}' Q(\mathbf{r}, \mathbf{r}') \left[\alpha \hat{\mathcal{L}}(\mathbf{r}', t) \phi(\mathbf{r}') - \beta \hat{\mathcal{M}}(\mathbf{r}', t) \phi^*(\mathbf{r}') \right] \\ &= \alpha \hat{\mathcal{L}}(\mathbf{r}', t) \phi(\mathbf{r}') - \beta \hat{\mathcal{M}}(\mathbf{r}', t) \phi^*(\mathbf{r}') \\ &\quad - \phi(\mathbf{r}) \int d\mathbf{r}' \phi^*(\mathbf{r}') \left[\alpha \hat{\mathcal{L}}(\mathbf{r}', t) \phi(\mathbf{r}') - \beta \hat{\mathcal{M}}(\mathbf{r}', t) \phi^*(\mathbf{r}') \right].\end{aligned}$$

Multiplying both sides by ϕ^* , and integrating over all space, we find [in view of the orthonormality of ϕ and of the orthogonality condition (4)] that

$$\begin{aligned}\epsilon_0 &= \phi(\mathbf{r}) \int d\mathbf{r}' \phi^*(\mathbf{r}') \left[\alpha \hat{\mathcal{L}}(\mathbf{r}', t) \phi(\mathbf{r}') - \beta \hat{\mathcal{M}}(\mathbf{r}', t) \phi^*(\mathbf{r}') \right] \\ &\quad - \phi(\mathbf{r}) \int d\mathbf{r}' \phi^*(\mathbf{r}') \left[\alpha \hat{\mathcal{L}}(\mathbf{r}', t) \phi(\mathbf{r}') - \beta \hat{\mathcal{M}}(\mathbf{r}', t) \phi^*(\mathbf{r}') \right] \\ &= 0.\end{aligned}$$

We have thus shown in the time-independent case for this formalism that there exists a zero-energy eigenvalue. However, the existence of a zero-energy eigenvalue does not imply that the Pine-Hughenoltz theorem [13] is satisfied or indeed that this corresponds to the Goldstone mode, nor is the remainder of the energy spectrum “corrected,” and is quite similar to the standard HFB spectrum in spite of the existence of a zero-energy eigenvalue.

We now obtain from the modified GGPE (15), the continuity equation for the condensate density

where

$$\mathbf{j}(\mathbf{r}, t) \equiv \frac{i\hbar}{2m} (\Phi(\mathbf{r}, t) \nabla \Phi^*(\mathbf{r}, t) - \Phi^*(\mathbf{r}, t) \nabla \Phi(\mathbf{r}, t)) \quad (29)$$

is the current density, and where we have defined the quantity

$$C(\mathbf{r}, t) = g \left(\tilde{m}(\mathbf{r}, t) \Phi^{*2}(\mathbf{r}, t) - \tilde{m}^*(\mathbf{r}, t) \Phi^2(\mathbf{r}, t) \right) + G^*(\mathbf{r}, t) - G(\mathbf{r}, t) \quad (30)$$

with

$$G(\mathbf{r}, t) \equiv \Phi^*(\mathbf{r}, t) \int d\mathbf{r}' \hat{P}(\mathbf{r}', \mathbf{r}, t) \phi(\mathbf{r}', t), \quad (31)$$

and use this to find an expression for the precessional frequencies of off-axis vortices and vortex arrays in quasi-two-dimensional BECs. To do this we consider a stationary vortex system in the frame rotating at the precessional frequency of the vortex or vortices.

III. CALCULATION OF PRECESSIONAL FREQUENCIES OF VORTICES IN QUASI-TWO-DIMENSIONAL BECS

In the quasi-2D regime, the time-independent orthogonal HFB equations in a frame rotating with angular frequency Ω are given in polar coordinates by the time-independent GGPE

$$\begin{aligned} \mu\Phi &= \left(\hat{h}_\Omega + C_{2D} \left(|\Phi|^2 + 2\tilde{n} \right) \right) \Phi + C_{2D} \tilde{m} \Phi^* \\ &\quad - \int_0^{2\pi} \int_0^\infty r' dr' d\theta' \hat{P}(r', \theta', r, \theta) \phi(r', \theta') \end{aligned} \quad (32)$$

and the 2D time-independent Bogoliubov de Gennes Equations (BdGEs)

$$\epsilon_q \mathbf{w}_q(r, \theta) = \int_0^{2\pi} \int_0^\infty r' dr' d\theta' \hat{\mathbf{L}}(r, \theta, r', \theta') \mathbf{w}_q(r', \theta') \quad (33)$$

where

$$\mathbf{w}_q(r, \theta) \equiv \begin{bmatrix} u_q(r, \theta) \\ v_q(r, \theta) \end{bmatrix} \quad (34)$$

and

$$\hat{\mathbf{L}}(r, \theta, r', \theta') \equiv \begin{bmatrix} \hat{\mathcal{L}}(r, \theta, r', \theta') & \hat{\mathcal{M}}(r, \theta, r', \theta') \\ -\hat{\mathcal{M}}^*(r, \theta, r', \theta') & -\hat{\mathcal{L}}^*(r, \theta, r', \theta') \end{bmatrix}. \quad (35)$$

Here we have defined the operators

$$\begin{aligned} \hat{\mathcal{L}}(r, \theta, r', \theta') &\equiv Q(r, \theta, r', \theta') \hat{\mathcal{L}}(r', \theta') \\ \hat{\mathcal{M}}(r, \theta, r', \theta') &\equiv Q(r, \theta, r', \theta') \hat{\mathcal{M}}(r', \theta') \end{aligned} \quad (36)$$

and

$$\begin{aligned} \hat{P}(r', \theta', r, \theta) &\equiv \left(\tilde{n}(r', \theta', r, \theta) \hat{\mathcal{L}}(r', \theta') \right. \\ &\quad \left. + \tilde{m}(r', \theta', r, \theta) \hat{\mathcal{M}}^*(r', \theta') \right) / \sqrt{N_c(t)} \end{aligned} \quad (37)$$

with

$$\begin{aligned} \hat{\mathcal{L}}(r, \theta) &\equiv \hat{h}_\Omega(r, \theta) - \mu + 2C_{2D} \left(|\Phi(r, \theta)|^2 + \tilde{n}(r, \theta) \right) \\ \hat{\mathcal{M}}(r, \theta) &\equiv C_{2D} \left(\Phi^2(r, \theta) + \tilde{m}(r, \theta) \right), \end{aligned} \quad (38)$$

$$Q(r, \theta, r', \theta') \equiv \frac{1}{r'} \delta(r - r') \delta(\theta - \theta') - \phi(r, \theta) \phi^*(r', \theta'), \quad (39)$$

and

$$\hat{h}_\Omega(r, \theta) = - \left(\frac{\partial^2}{\partial r^2} + \frac{1}{r} \frac{\partial}{\partial r} + \frac{1}{r^2} \frac{\partial^2}{\partial \theta^2} \right) + i\Omega \frac{\partial}{\partial \theta} + r^2. \quad (40)$$

We note that in the quasi-2D regime that Ω reduces to the component $\Omega \equiv \Omega_z$ along the z -axis. We use the dimensionless units $r_0 = \sqrt{\frac{\hbar}{m\omega_r}}$ for the length scale, and $t_0 = \frac{2}{\omega_r}$ for the time scale, and express the condensate wave function and quasiparticle amplitudes in units of \sqrt{N}/r_0^3 . Then the energies are given in harmonic oscillator units $\hbar\omega_r/2$. The nonlinearity constant

C_{2D} is found by expressing the interaction term g in dimensionless units, and integrating over all z yielding $C_{2D} = 8\pi \left(\frac{\lambda}{2\pi}\right)^{1/2} \frac{a_s}{r_0} N$ where N is the number of atoms, a_s is the scattering length, and $\lambda \equiv \omega_z/\omega_r$ is the trap aspect ratio.

Let $R(\mathbf{r}) \equiv \text{Re}(\Phi(\mathbf{r}))$ and $I(\mathbf{r}) \equiv \text{Im}(\Phi(\mathbf{r}))$. Then in the two-dimensional system, the continuity equation for the condensate density is given by

$$\Omega r^2 A(r, \theta) = B(r, \theta) \quad (41)$$

where we have defined

$$A(r, \theta) \equiv \left(R \frac{\partial R}{\partial \theta} + I \frac{\partial I}{\partial \theta} \right), \quad (42)$$

and

$$\begin{aligned} B(r, \theta) &\equiv \left[r^2 \left(R \frac{\partial^2 I}{\partial r^2} - I \frac{\partial^2 R}{\partial r^2} \right) + r \left(R \frac{\partial I}{\partial r} - I \frac{\partial R}{\partial r} \right) \right. \\ &\quad \left. + \left(R \frac{\partial^2 I}{\partial \theta^2} - I \frac{\partial^2 R}{\partial \theta^2} \right) \right] + i \frac{r^2}{2} C(r, \theta). \end{aligned} \quad (43)$$

with

$$\begin{aligned} C(r, \theta) &\equiv C_{2D} \left(\tilde{m}(r, \theta) \Phi^{*2}(r, \theta) - \tilde{m}^*(r, \theta) \Phi^2(r, \theta) \right) \\ &\quad + G^*(r, \theta) - G(r, \theta) \end{aligned} \quad (44)$$

and

$$G(r, \theta) \equiv \Phi^*(r, \theta) \int_0^{2\pi} \int_0^\infty r' dr' d\theta' \hat{P}(r', \theta', r, \theta) \phi(r', \theta'). \quad (45)$$

Multiplying both sides by $A(r, \theta)$, and integrating over all space gives us the expression

$$\Omega = \frac{\int_0^{2\pi} \int_0^\infty A(r, \theta) B(r, \theta) r dr d\theta}{\int_0^{2\pi} \int_0^\infty r^2 [A(r, \theta)]^2 r dr d\theta} \quad (46)$$

which we solve self-consistently with the time-independent orthogonal HFB equations in the frame rotating at angular frequency Ω . The converged solution then represents a stationary solution in the rotating frame, and Ω corresponds to the precessional frequency of the off-axis vortex or vortex array.

A vortex at position (r_1, θ_1) may be created by expanding the condensate wave function in terms of modified Laguerre basis functions $\{\chi_{ln}^{(1)}(r, \theta)\}$ as follows:

Define

$$\mathcal{S}^{(1)} \equiv \{l, n \mid (l, n) \in \mathcal{S} - \{(1, 0)\}\} \quad (47)$$

where $\mathcal{S} \equiv \{l, n \mid n = 0, \dots, l = 0, \pm 1, \dots\}$, then

$$\Phi(r, \theta) = \sum_{l, n \in \mathcal{S}^{(1)}} a_{ln} \chi_{ln}^{(1)}(r, \theta) \quad (48)$$

provided (r_1, θ_1) is not a root of $\xi_{ln}(r, \theta)$, where we define

$$\chi_{ln}^{(1)}(r, \theta) \equiv \xi_{ln}(r, \theta) - \frac{\xi_{ln}(r_1, \theta_1)}{\xi_{10}(r_1, \theta_1)} \xi_{10}(r, \theta), \quad (49)$$

with

$$\xi_{ln}(r, \theta) = \frac{e^{il\theta}}{\sqrt{2\pi}} \left(\frac{2n!}{(n+|l|)!} \right)^{1/2} e^{-r^2/2} r^{|l|} L_n^{|l|}(r^2), \quad (50)$$

and $L_n^{|l|}(x)$ a modified Laguerre polynomial of order n . The superscript in the representation of the modified basis function, indicates a single vortex. This is motivated simply by expanding the condensate wave function in terms of the complete Laguerre basis $\{\xi_{ln}(r, \theta) \mid l, n \in \mathcal{S}\}$ and considering that $\Phi(r_1, \theta_1) = \sum_{ln} a_{ln} \xi_{ln}(r_1, \theta_1) = 0$. Imposing this condition implies dependency of one of the coefficients a_{ln} on the others, reducing the dimension of the vector space by one. Here we choose to represent a_{10} in terms of the remainder $\{a_{ln} \mid l, n \in \mathcal{S}^{(1)}\}$. We find that $a_{10} = -\sum_{l,n \in \mathcal{S}^{(1)}} (\xi_{ln}(r_1, \theta_1)/\xi_{10}(r_1, \theta_1)) a_{ln}$, hence we can write $\Phi(r, \theta)$ in the form (48).

This procedure may be extended to N_v vortices $\{(r_1, \theta_1), \dots, (r_{N_v}, \theta_{N_v})\}$ by an iterative process, writing

$$\Phi(r, \theta) = \sum_{l,n \in \mathcal{S}^{(N_v)}} a_{ln} \chi_{ln}^{(N_v)}(r, \theta) \quad (51)$$

where we have defined

$$\chi_{ln}^{(N_v)}(r, \theta) \equiv \chi_{ln}^{(N_v-1)}(r, \theta) - \frac{\chi_{ln}^{(N_v-1)}(r_{N_v}, \theta_{N_v})}{\chi_{N_v,0}^{(N_v-1)}(r_{N_v}, \theta_{N_v})} \chi_{N_v,0}^{(N_v)}(r, \theta), \quad (52)$$

and where we have generalized the definition (47) in the single-vortex case to

$$\mathcal{S}^{(N_v)} \equiv \{l, n \mid (l, n) \in \mathcal{S} - \{(1, 0), \dots, (N_v, 0)\}\} \quad (53)$$

in the multi-vortex case.

We illustrate the method by considering a dilute Bose gas consisting of 2000 ^{87}Rb atoms in an axially symmetric harmonic trap, with radial and axial harmonic trapping frequencies of $\Omega_r = 2\pi \times 10\text{Hz}$ and $\Omega_z = 2\pi \times 400\text{Hz}$, respectively. Thus the axial confinement is sufficiently strong that all excited axial states may be neglected, hence the axial (z) component can then be integrated out, and the BEC may effectively be treated as two-dimensional. In order for this quasi-two-dimensional approximation to hold, we require that the axial harmonic transition energy $\hbar\omega_z$ be much greater than the temperature T and the mean-field energy of the BEC [14]. Here the axial harmonic energy transition corresponds to a temperature of $T_{\Delta_z} = \hbar\omega_z/k_B = 19.2\text{nK}$, and the mean-field energy to an effective temperature of $T_{MF} = C_{2D} n_0^{(2D)}/k'_B = .84\text{nK}$, where k_B is Boltzmann's constant, and $k'_B = 2k_B/\hbar\omega_r$. In all these simulations the BEC temperature $T \leq 10\text{nK}$, so this approximation is justified.

Stationary solutions are found in the case of a single off-axis vortex, and in the cases of triangular and hexagonal vortex arrays, provided the interactions between the vortices are not too strong. In cases where there are strong interactions between vortices, approximately stationary solutions can be found, establishing

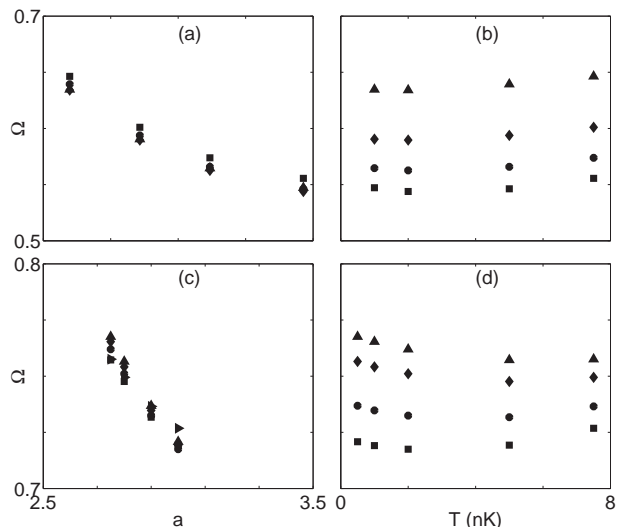


FIG. 1: Triangular vortex array. (a) Precessional frequency Ω versus lattice parameter a at temperatures 1, 2, 5 and 7.5 nK (triangles, diamonds, circles, squares); (b) precessional frequency Ω versus temperature T for lattice parameter $1.5\sqrt{3}$, $1.65\sqrt{3}$, $1.8\sqrt{3}$, and $2\sqrt{3}$ (triangles, diamonds, circles, squares). Hexagonal vortex array. (c) Precessional frequency Ω (in units of radial trapping frequency ω_r) versus lattice parameter a at temperatures 1, 2, 5 and 7.5 nK (triangles, diamonds, circles, squares); (d) precessional frequency Ω versus temperature T for lattice parameter 2.75, 2.8, 2.9 and 3 (triangles, diamonds, circles, squares). All frequencies are in units of the radial trapping frequency ω_r . All positions are in units of the harmonic oscillator length r_0 .

lower and upper bounds for the precessional frequency, and the precessional frequency determined more accurately in time-dependent simulations.

Precessional frequencies as a function of vortex position a and of temperature T for the single off-axis case are presented in Figs. 1(c) and (d) of a previous publication [15], and will not be repeated here. Instead, we concentrate on the cases of triangular and hexagonal vortex arrays. The precessional frequency Ω as a function of temperature T for various values of lattice parameter a and of lattice parameter a at various temperatures are shown in Figs. 1(a) and 1(b) for the triangular vortex array and in Figs. 1(c) and 1(d) for the hexagonal vortex array. We see that Ω decreases with increasing lattice parameter a over the range shown (within the Thomas-Fermi radius). This is in accord with the areal density law given by the approximation [7]

$$\Omega = \frac{\hbar\pi}{m} \left[n_v + \frac{1}{2\pi} \frac{R_{TF}^2}{(R_{TF}^2 - r^2)^2} \ln \left(e^{-1} \frac{\omega_r}{\Omega} \right) \right] \quad (54)$$

where n_v is the areal density of vortices approximated by $n_v = N_v/(\pi R_{TF}^2)$, N_v is the number of vortices in the vortex array, and R_{TF} is the Thomas-Fermi radius and may be understood by considering that the vortex precession velocity is determined primarily by the back-

ground velocity field around the vortex core, and the core shape [16, 17]. The effect of their image charges in the condensate boundary is less important, in contrast with the single vortex case [18, 19]. In the single off-axis case Ω increases with increasing a [15]. This is in agreement with GPE results [18, 19] and may be explained in terms of the effect of the vortex's image charge in the boundary of the condensate [18, 19].

Figures 2(a) and 2(b) show, respectively, simulated absorption images for the condensate density and the thermal density [20], and Fig. 2(c) the condensate phase in the xy -plane for a single off-axis vortex situated at $a = 0.5$. We note the phase singularity in Fig. 2(c) indicating a singly charged vortex. Similarly Figs. 2(d) and 2(e) show, respectively, simulated absorption images for the condensate density and the thermal density, and Fig. 2(f) shows the condensate phase in the xy -plane for a triangular vortex lattice having lattice parameter $a = 1.65\sqrt{3}$. Figs. 2(g)-2(i) show the respective plots for a hexagonal vortex lattice having lattice parameter $a = 2.9$. The phase singularities in Figs. 2(f) and 2(i) indicate respectively, three and seven singly charged vortices. We note from the simulated absorption images for the condensate in Figs. 2(a), 2(d) and 2(g) that the condensate extends further outward for the triangular and hexagonal vortex arrays (i.e., larger Thomas-Fermi radius) than for the single vortex case. This is consistent with our findings concerning the dependency of Ω on a , where we find that Ω decreases with increasing a in the vortex array case, in contrast to the single off-axis vortex case. Unfortunately, it is not possible to find stationary solutions in the limit of sufficiently large numbers of vortices to validate against the areal density approximation [6, 8]; nevertheless we perform this calculation for the case of seven vortices.

Figures 3(a) and 3(b) represent plots of precessional frequency Ω versus lattice parameter a at temperatures $T = 2$ nK and $T = 5$ nK, respectively, for vortex arrays composed of two, three, and seven vortices. We see that Ω increases with an increasing number of vortices. The inserts of Figs. 3(a) and 3(b) seem to indicate that Ω tends asymptotically to an upper limit as the number of vortices increases, presumably the limit predicted by the areal density approximation (54). In the dimensionless units used here, this may be written

$$\Omega = \frac{1}{R_{TF}^2} \left[N_v + \frac{1}{2 \left(1 - \frac{r^2}{R_{TF}^2} \right)^2} \ln \left(e^{-1} \frac{\omega_r}{\Omega} \right) \right]. \quad (55)$$

Therefore, for the hexagonal array where $N_v = 7$, and taking $R_{TF} \sim 3.5r_0$, we predict to first approximation a precessional frequency of $\Omega \sim .57\omega_r$. Taking into account the second term in (55) with $r \sim 0.5R_{TF}$, we predict $\Omega \sim .55\omega_r$ (so the second term is unimportant in the regime considered here). This is of the order of 20% lower than the value predicted using the continuity equation calculation. We note that the areal density approximation is valid only for a large number of vortices.

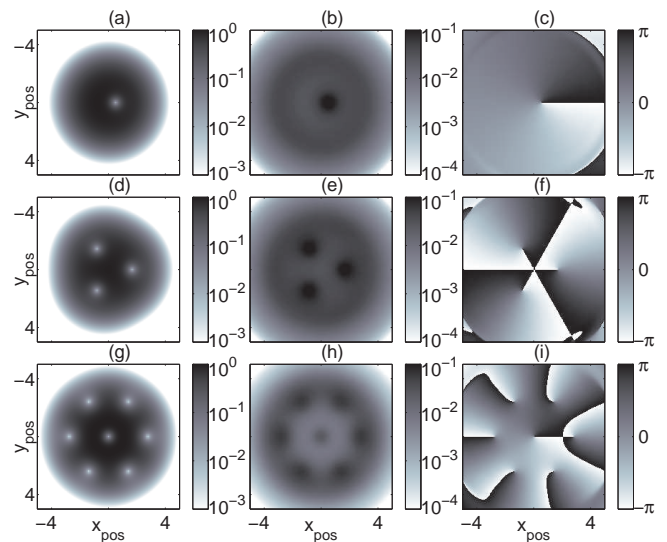


FIG. 2: Simulated absorption images [20] for off-axis vortex, triangular vortex array and hexagonal vortex array showing (a) condensate density, (b) thermal density, (c) condensate phase for a single vortex at $a = 0.5$, and (d) condensate density, (e) thermal density, (f) condensate phase for a triangular vortex array with lattice parameter $a = 1.65\sqrt{3}$, and (g) condensate density, (h) thermal density, (i) condensate phase for a hexagonal vortex array with lattice parameter $a = 2.9$. All positions are in units of the harmonic oscillator length r_0 .

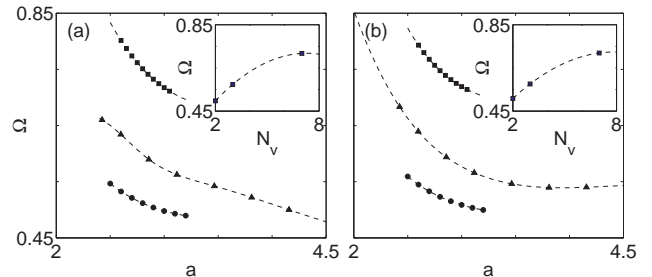


FIG. 3: Precessional frequency Ω versus lattice parameter a for vortex arrays composed of two (circles), three (triangles), and seven vortices (squares) with cubic spline interpolation (dashed line) (a) at $T = 2$ nK, and (b) at $T = 5$ nK. The insert in each respective figure shows the precessional frequency Ω versus number of vortices for vortex arrays composed of two, three, and seven vortices having lattice parameter $a = 3.0$ with cubic spline interpolation (dashed line). All frequencies are in units of the radial trapping frequency ω_r . All positions are in units of the harmonic oscillator length r_0 .

Furthermore, referring to the inserts of Figs. 3(a) and (b) reveals that the precessional frequency approaches an asymptotic value of $\sim .72$. We conclude, however, that these results are consistent in the asymptotic limit.

IV. EVOLUTION OF TIME-INDEPENDENT SOLUTIONS

Time-dependent simulations using the time-independent data initial state are in good agreement with the above calculations. For a single vortex at $a = 0.5$ radial harmonic oscillator units from the axis, the precessional frequency was estimated using a least-squares fit of a sinusoid to the vortex x -displacement versus time and was found to be $\Omega_{LS} = 0.3794\omega_r$, in good agreement with the value of $\Omega = 0.3727\omega_r$, as predicted in the time-independent calculations. The error in the prediction scales as the number of computational basis functions which, for practical reasons, is only 209 in these calculations. For 839 computational basis functions, the time-independent calculations predict a value of $\Omega = 0.3761\omega_r$. We see no evidence of dissipation during the time of the simulation of five trap cycles, and the results reveal that the trajectory of the vortex constitutes a circle.

Time-dependent simulations were also performed at $T = 5$ nK for a symmetrical triangular vortex array with lattice parameter $a = 1.65\sqrt{3}$ (i.e., three vortices symmetrically positioned at 1.65 radial harmonic oscillator units from the axis), and for a symmetrical hexagonal triangular vortex centered on the axis having lattice parameter $a = 2.85$ (i.e., seven vortices), again using time-independent calculations for the initial state. In both simulations, the off-axis vortices precess in a circle, and again we see no evidence of dissipation during the time of the simulation of five trap cycles. The precessional frequency $\Omega_{LS} = 0.5856\omega_r$ for the triangular vortex array was estimated using a least squares fit as before, in good agreement with the value of $\Omega = 0.5938\omega_r$, as predicted in the time-independent calculations for 209 computational basis functions.

V. STIRRING OF THE CONDENSATE

In these, and in other time-dependent simulations, the temperature T remains fixed. It is not necessary to vary μ to maintain particle conservation since the rate of change in the condensate population dN_c/dt and in the non-condensate population $d\tilde{N}/dt$ are equal and opposite, depending only on \tilde{m} and Φ , i.e., $dN_c/dt = -d\tilde{N}/dt = i\frac{q}{\hbar} \int d\mathbf{r} (\tilde{m}\Phi^{*2} - \tilde{m}^*\Phi^2)$, therefore particle conservation always holds. In these simulations we use one or more Gaussian rotating potentials in order to stir the condensate. The stirring imparts angular momentum to the condensate, and therefore one would expect the production of vortices in cases where the angular frequency of the stirrer(s) exceeds a certain critical value. This should correspond (at least approximately) to the velocity of the stirrer with respect to the fluid exceeding the local Landau critical velocity (i.e. the local speed of sound). In what follows we shall establish a critical stir-

ring frequency, below which no vortices are produced in regions of appreciable density (i.e., within the Thomas-Fermi radius). In these simulations we find that this critical frequency corresponds to a velocity of the stirrer through the BEC that is slightly in excess of the local Landau critical velocity (see Table 1). In the simulations where the critical stirring frequency is exceeded, we are able to determine by the method of least squares, as alluded to above, the precessional frequencies and compare these with the values predicted in the time-independent calculations using the continuity equation for the condensate density. We shall see presently that the agreement between the time-dependent values and the predicted values using the time-independent calculations is good, as one would expect in the adiabatic case since then the term $i\hbar\frac{\partial}{\partial t}|\Phi|^2$ in the time-dependent continuity equation for the condensate density (28) would be small, i.e., of order of the fluctuations in the chemical potential. We stir the BEC using a single Gaussian stirrer at $a = 1.5r_0$ off axis, of amplitude $10\hbar\omega_r/2$, full width at half maximum (FWHM) $0.82r_0$. Two cases are considered. In the first we stir the BEC at a sub-critical stirring frequency $0.38\omega_r$, with the stirrer on for 10 trap cycles. In the second case we stir the BEC with stirring frequency $\Omega = 0.5\omega_r$, with the stirrer on for 4.5 trap cycles. In both cases the stirring frequency is ramped up from zero to the specified value over 0.2 trap cycles. In the second case two vortices are produced, and the simulated absorption images are shown in Fig. 4, and the trajectories of these vortices in Fig. 5 [21]. Figure 6 I(a) shows the condensate, thermal, and total angular momentum in the first case where the stirring frequency ($\Omega = 0.38\omega_r$) is sub-critical, and Fig. 6II(a) in the second case where $\Omega = 0.5\omega_r$ which is above the critical stirring frequency, and where two vortices are produced as shown in Figs. 4 and 5. In the case of the first simulation, the rotational frequency Ω is sub-critical, so no vortices are produced within the Thomas Fermi radius, therefore negligible angular momentum is transferred to the condensate. This angular momentum is due to circulation corresponding to vortices in regions of negligible density. We see in both cases that a small amount of angular momentum is also transferred to the thermal cloud. We note that L_z remains fixed once the stirring ceases after 10.2 trap cycles in the first case, and 4.7 trap cycles in the second in accordance with the conservation of angular momentum. We note in the first case where the stirring frequency is subcritical that the angular momentum for the thermal population increases for the first few trap cycles, reaching a saturation value after $\sim 4 \rightarrow 5$ trap cycles. Simulations over a much longer time scale (not presented here) reveal a slow cyclical change in the thermal population angular momentum of a few percentage points. Once the stirrer is switched off, we see a steady increase in the thermal population angular momentum with a resultant loss in the angular momentum of the condensate (since the overall angular momentum is conserved). During the time of stirring, the condensate

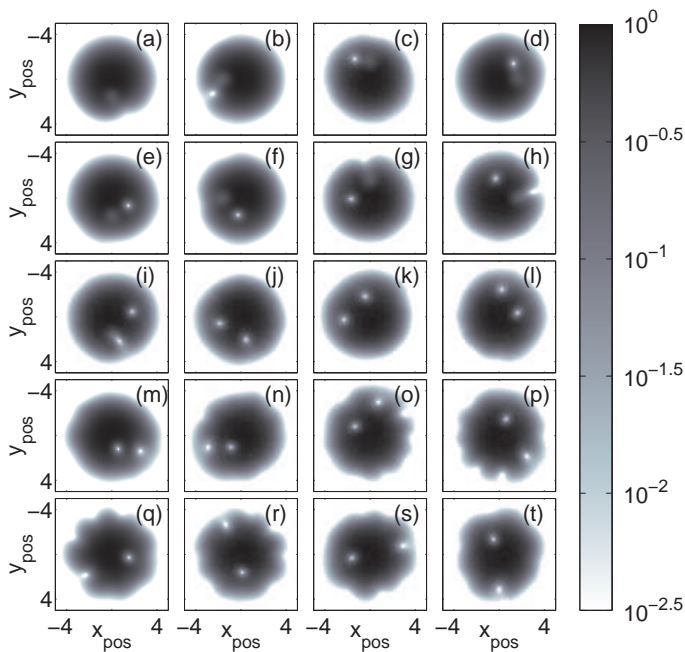


FIG. 4: Simulated absorption images [20]; stirring of condensate in an counterclockwise direction using one Gaussian stirrer at $a = 1.5 r_0$ off axis, of amplitude $10 \hbar \omega_r / 2$, FWHM $0.82 r_0$, switched on adiabatically over 0.2 trap cycles, stirring frequency $0.5 \omega_r$, stirrer on for 4.5 trap cycles after (a) 0.5, (b) 1, (c) 1.5, (d) 2, (e) 2.5, (f) 3, (g) 3.5, (h) 4, (i) 4.5, (j) 5, (k) 5.5, (l) 6, (m) 6.5, (n) 7, (o) 7.5, (p) 8, (q) 8.5, (r) 9, (s) 9.5, and (t) 10 trap cycles. All positions are in units of the harmonic oscillator length r_0 .

angular momentum varies cyclically corresponding to the variation of the distance of vortices from the axis (see also Ref. [22]). In the case where the stirring frequency is subcritical, these vortices would lie outside the Thomas-Fermi radius, and would therefore be subthreshold. Figs. 6I(b) and 6II(b) show, respectively, the changes in condensate and thermal populations, where we see rigorous observance of particle number conservation. In order to understand why there exists a critical frequency for the production of vortices within the Thomas-Fermi radius, we calculate the Landau critical velocity v_{LC} given by the local speed of sound at the point of the stirrer $s = \sqrt{ng/m}$, where n is the density of the condensate and m is the mass of a particle. We use the local density approximation and calculate the speed of sound s at the stirrer using the local density n of the superfluid at the point of the stirrer. In these simulations, we measure the two-dimensional density $n^{(2D)}$ where we have integrated out the axial component, assuming the axial confinement is sufficiently tight that all axial modes except the lowest can be ignored, and we can write the local Landau critical frequency in terms of the local two-dimensional density $n^{(2D)}$ as $V_{LC} = \sqrt{2\sqrt{2}C_{2D}n^{(2D)}}$. The speed of the stirrer is given by $v_{\text{stir}} = 2\pi r_s \Omega_s$ for a stirrer at radius r_s rotating at angular frequency Ω_s . We can rewrite

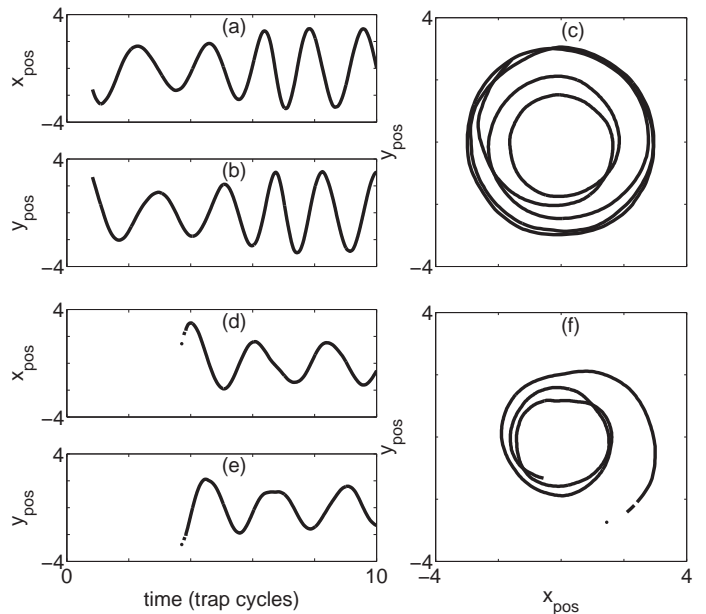


FIG. 5: Stirring of condensate using one Gaussian stirrer at $a = 1.5 r_0$ off axis, of amplitude $10 \hbar \omega_r / 2$, FWHM $0.82 r_0$, switched on adiabatically over 0.2 trap cycles, stirring frequency $0.5 \omega_r$, stirrer on for 4.5 trap cycles (a) x -displacement of vortex 1, (b) y -displacement of vortex 1, and (c) trajectory of vortex 1 over a period of 10 trap cycles (d) x -displacement of vortex 2, (e) y -displacement of vortex 2, and (f) trajectory of vortex 2 over a period of 10 trap cycles. All positions are in units of the harmonic oscillator length r_0 .

$\Omega(\omega_r)$	v_{stir}/v_{LC}	$L_z(N\hbar)$
0.38	1.12	0.035
0.39	1.15	0.045
0.4	1.18	0.5 (varies between ~ 0.25 and ~ 0.7)
0.45	1.33	0.55 (varies between ~ 0.3 and ~ 0.8)
0.5	1.48	0.6 for one vortex, ~ 0.8 for two vortices and ~ 2.2 for three vortices

TABLE I: Relationship of the local stirrer velocity with the average z -component of the angular momentum \bar{L}_z for time-dependent HFB simulations. The Landau critical velocity is that corresponding to the density at the stirrer location, and $n^{(2D)} = 0.02 r_0^{-2}$.

this in terms of the Landau critical velocity as

$$v_{\text{stir}} = \frac{2\pi r_s \Omega_s}{\sqrt{2\sqrt{2}C_{2D}n^{(2D)}}} v_{LC}. \quad (56)$$

Table 1 shows numerically calculated values of the time-averaged z -component quantum expectation value of the angular momentum \bar{L}_z and how this is related to the local stirring velocity in units of the Landau critical velocity for the stirring angular frequencies 0.39, 0.4, 0.45, and $0.5 \omega_r$. We see evidence of a critical stirring angular velocity between 0.39 and $0.4 \omega_r$ corresponding to a local stirrer velocity just slightly above the Landau critical velocity. These results are consistent with simple GPE

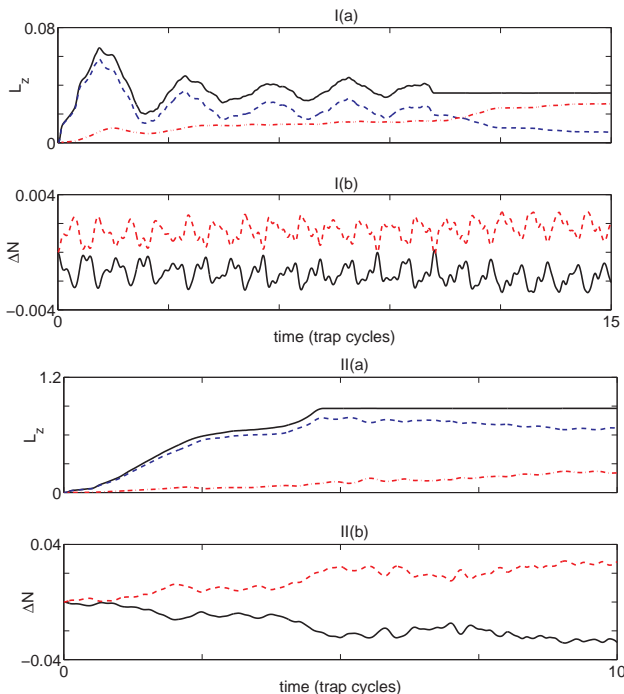


FIG. 6: (Color online) Stirring of condensate (I) using one Gaussian stirrer at $a = 1.5r_0$ off axis, of amplitude $10 \hbar\omega_r/2$, FWHM $0.82 r_0$, switched on adiabatically over 0.2 trap cycles, stirring frequency $0.38 \omega_r$, stirrer on for 10 trap cycles, and (II) using one Gaussian stirrer at $a = 1.5r_0$ off axis, of amplitude $10 \hbar\omega_r/2$, FWHM $0.82 r_0$, switched on adiabatically over 0.2 trap cycles, stirring frequency $0.5 \omega_r$, stirrer on for 4.5 trap cycles showing (a) z component of total angular momentum (solid line), condensate angular momentum (dashed line), and thermal population angular momentum (dash-dotted line) versus time, (b) change in thermal population and condensate population (solid line) versus time. The change in the populations ΔN is given in units of the number of atoms N . All angular momenta are in units of $N\hbar$.

simulations (results not presented here).

No experiments have been performed on stirring a BEC using a narrow rotating probe as considered here but experiments [23] have been performed that show evidence of a critical stirring angular velocity using elliptical deformation of the trap. Experiments to test the superfluid critical velocity using the linear motion of a narrow probe laser beam have also been performed [24–26], finding critical velocities for the onset of dissipation $\sim 5 - 10$ times smaller than the critical velocity inferred from the bulk Bogoliubov speed of sound. Time-dependent GPE simulations [27] also indicate that dissipation first occurs at speeds significantly less than the speed of sound. However, the linear motion of the probe in these works excite vortex dipole or solitons, and are not therefore directly applicable to the present work.

In a previous study [22], similar stirring simulations were carried out using time-dependent GPE simulations. However, the critical stirring frequency referred to in these results are the thermodynamic critical frequency

(at which the vortex-free and central vortex states have equal energies), whereas the results presented here refer to the critical frequency at which vortices are created within the Thomas-Fermi radius. Nevertheless, the results of Ref. [22] are consistent with the simulations performed in this work.

The precessional frequencies for single off-axis vortices were obtained for simulations deploying the single stirrer at $\Omega = 0.5\omega_r$ for 2.5 trap cycles. Least squares analysis of the vortex trajectories as described above reveals that the vortex in the second simulation developed at a distance of ~ 1.7 harmonic oscillator units from the axis, with a precessional frequency of $\sim 0.42\omega_r$, in very good agreement with the off-axis time-independent calculations (see Figs. 1(c) and 1(d) in Ref. [15]).

In order to test the predicted precessional frequencies for triangular vortex arrays, three equi-spaced Gaussian stirrers at $a = 1.5 r_0$ off axis, of amplitude $10 \hbar\omega_r/2$ (i.e. of the same order as the chemical potential, $\mu \gtrsim 10\hbar\omega_r/2$), FWHM $0.82 r_0$, stirring frequency ramped up from zero to $0.5\omega_r$ over 0.2 trap cycles, are used to stir the BEC for 2.5 trap cycles. Thus a symmetrical triangular vortex array was produced. The least-squares estimates of the precessional frequency of $\Omega_{LS} = 0.7\omega_r$, are in very good agreement with the interpolated values from Figs. 1(a) and 1(b) of $\Omega \sim 0.7 \omega_r$.

The above results for the stirring simulations indicate very good agreement with the values predicted using the continuity equation for the condensate density in the time-independent calculations. These results were attained in the case where the stirrers were introduced adiabatically. It should be noted that the reason for using three Gaussian stirrers, as opposed to just one, is not that we need three stirrers to create three vortices (one stirrer is sufficient for this purpose provided the BEC is stirred long enough at a sufficiently high frequency), but rather in order to create a symmetrical triangular vortex array so the time-independent predictions can be tested.

VI. BREAKING OF THE AXIAL SYMMETRY OF THE TRAPPING POTENTIAL

Noether's theorem [28] states that in a conservative physical system, a differentiable symmetry of the Lagrangian (and, it can be shown, of the Hamiltonian) has a conserved quantity associated with the system (i.e. a corresponding conservation law). In this case the axial symmetry of the trapping potential implies the conservation of the axial component (i.e., the z -component) of the angular momentum. The quantum expectation value of the angular momentum is given by $\langle \mathbf{L} \rangle = \int d\mathbf{r} \langle \hat{\psi}^\dagger \hat{\mathbf{L}} \hat{\psi} \rangle$, where $\hat{\psi} = \hat{\Phi} + \hat{\eta}$ as above. Thus using the expression

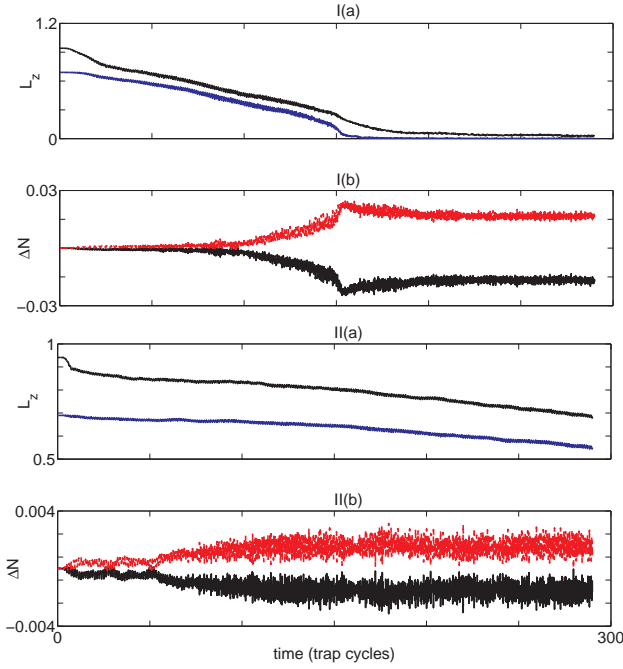


FIG. 7: (Color online) Breaking of axial symmetry; (I) for single off-axis vortex for turn-on time of 20 trap cycles for eccentricity parameter $\epsilon = 0.25$, and (II) for single off-axis vortex for turn-on time of 20 trap cycles for eccentricity parameter $\epsilon = 0.1$ showing (a) z -component of total angular momentum and condensate angular momentum (lower line) versus time and (b) change in thermal population and condensate population (lower line) versus time. The change in the populations ΔN is given in units of the number of atoms N . All angular momenta are in units of $N\hbar$.

(22) for the non-condensate density matrix, we find that

$$\langle \mathbf{L} \rangle = -i\hbar \int d\mathbf{r} \left[\Phi^* (\mathbf{r} \times \nabla) \Phi + \sum_q (n_q u_q^* (\mathbf{r} \times \nabla) u_q + (n_q + 1) v_q (\mathbf{r} \times \nabla) v_q^*) \right]. \quad (57)$$

It can be shown from the time-dependent HFB equations (15) and (16) that

$$\frac{d\langle \mathbf{L} \rangle}{dt} = \int d\mathbf{r} \left(|\Phi|^2 + \tilde{n} \right) \hat{\mathbf{L}} V_T. \quad (58)$$

This determines the rate of change in angular momentum in the BEC system, and we see that $\frac{d}{dt} L_z = 0$ for an axially symmetric trapping potential in accordance with Noether's theorem. The implication of this is that when this symmetry is broken, L_z is no longer conserved, and since there is no external source of angular momentum here, we conclude that angular momentum will be lost since $\frac{d}{dt} L_z$ will now be non-zero by equation (58). This leads to vortex decay, and the vortex spirals outward as angular momentum is lost. This is in accordance with work done by Zhuravlev *et al.* [29] on the arrest of vortex arrays by a trap anisotropy, although this work deals with large vortex arrays, whereas the calculations performed here concern single off-axis vortices and

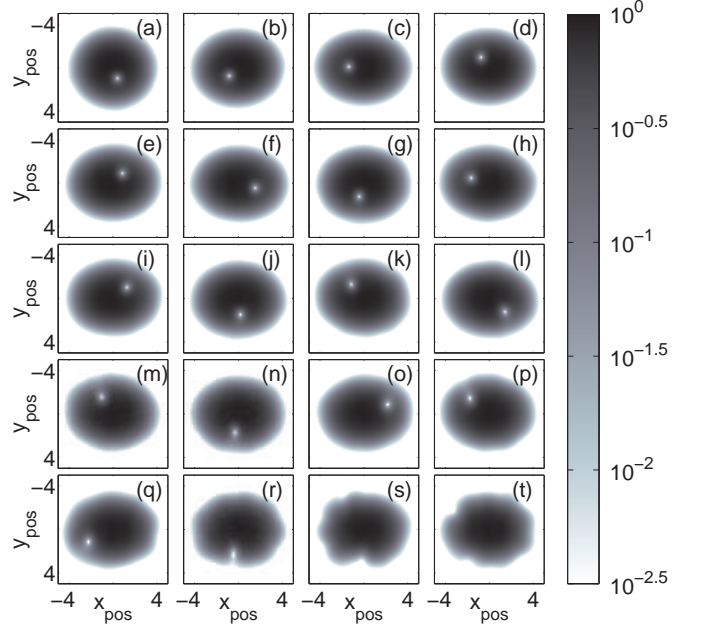


FIG. 8: Simulated absorption images [20] for breaking of axial symmetry with turn-on time of 20 cycles for single off-axis vortex for eccentricity parameter $\epsilon = 0.25$ after (a) 8, (b) 16, (c) 24, (d) 32, (e) 40, (f) 48, (g) 56, (h) 64, (i) 72, (j) 80, (k) 88, (l) 96, (m) 104, (n) 112, (o) 120, (p) 128, (q) 136, (r) 144, (s) 152, and (t) 160 trap cycles. All positions are in units of the harmonic oscillator length r_0 .

small vortex arrays. In order to test this, we introduce an eccentricity into the trapping potential, thereby breaking the axial symmetry. Initially the trapping potential is axially symmetric and the eccentricity introduced by means of the perturbation potential

$$V_{\text{pert}}(r, \theta) = \epsilon r^2 (\sin^2 \theta - \cos^2 \theta) \quad (59)$$

which is introduced adiabatically after two trap cycles over a period of 20 trap cycles. In these simulations, we introduce eccentricities of $\epsilon = 0.25$ and $\epsilon = 0.1$ in both the cases of a single off-axis vortex and of a triangular vortex array. In the single vortex case, the initial state consists of a BEC with a single precessing vortex situated at position $a = 1.1$ trap units from the axis. The z -component of the angular momentum L_z versus time in trap cycles is plotted in Figs. 7I(a) and 7II(a) for the cases of $\epsilon = 0.25$ and $\epsilon = 0.1$, respectively, where we see a decrease in L_z with time once the symmetry of the trapping potential has been broken. Figures 7I(b) and 7II(b) show the respective changes in the thermal and condensate populations, and reveal an increase in the thermal population as the vortex spirals outwards and finally decays. This is consistent with the notion that the vortex decays into excitations when it reaches the condensate boundary [30]. Simulated absorption images for $\epsilon = 0.25$ with turn-on time of 20 trap cycles are shown in Figs. 8(a)-8(t). In the simulations with $\epsilon = 0.25$ the lifetime of the vortex is approximately 145 to 150 trap

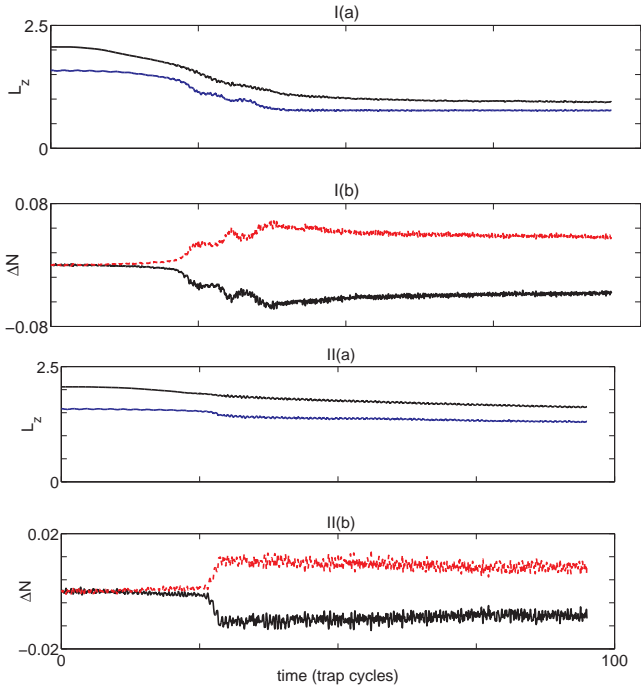


FIG. 9: (Color online) Breaking of axial symmetry, (I) for triangular vortex array for turn-on time of 20 trap cycles for eccentricity parameter $\epsilon = 0.25$, and (II) for triangular vortex array for turn-on time of 20 trap cycles for eccentricity parameter $\epsilon = 0.1$ showing (a) z -component of total angular momentum and condensate angular momentum (lower line) versus time and (b) change in thermal population and change in condensate population (lower line) versus time. The change in the populations ΔN is given in units of the number of atoms N . All angular momenta are in units of $N\hbar$.

cycles, and for $\epsilon = .1$ substantially larger, with an extrapolated value of the order of 700 trap cycles. The vortex precessional frequencies are in good agreement with the time-independent calculations, and we note that in all cases from the vortex trajectories that the vortices precess faster as they move outward [31], which, again, is in agreement with the time-independent results (see Fig. 1(c) of Ref. [15]), before finally decaying. This is also consistent with the reduction in angular momentum [see Figs. 7I(a) and 7II(a) for the cases of $\epsilon = 0.25$ and $\epsilon = 0.1$ respectively]. The vortex moves outwards and precesses faster as it does so in agreement with Fig. 1(c) of Ref. [15], accompanied by a loss in angular momentum [see Figs. 7I(a) and 7II(a)]. As discussed above, this loss of angular momentum is due to the symmetry breaking of the trap and the loss of the angular momentum is as given by (58). The loss of the vortex after $\sim 145 \rightarrow 150$ trap cycles (loss of tracking after ~ 146 trap cycles) for the case $\epsilon = 0.25$ is consistent with the decline in L_z seen in Fig. 7I(a) and the sudden increase in the thermal population in Fig. 7I(b) at ~ 150 trap cycles. These results are also in qualitative agreement with recent simulations using a classical field treatment comprising the projected

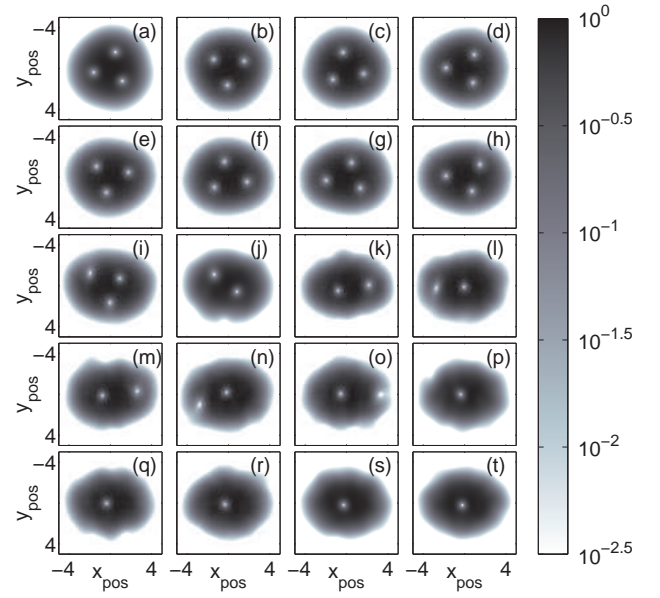


FIG. 10: Simulated absorption images [20] for breaking of axial symmetry for triangular vortex array over 20 trap periods with lattice parameter $a = 1.65\sqrt{3}$ for eccentricity parameter $\epsilon = 0.25$ after (a) 2.5, (b) 5, (c) 7.5, (d) 10, (e) 12.5, (f) 15, (g) 17.5, (h) 20, (i) 22.5, (j) 25, (k) 27.5, (l) 30, (m) 32.5, (n) 35, (o) 37.5, (p) 40, (q) 42.5, (r) 45, (s) 47.5, and (t) 50 trap cycles. All positions are in units of the harmonic oscillator length r_0 .

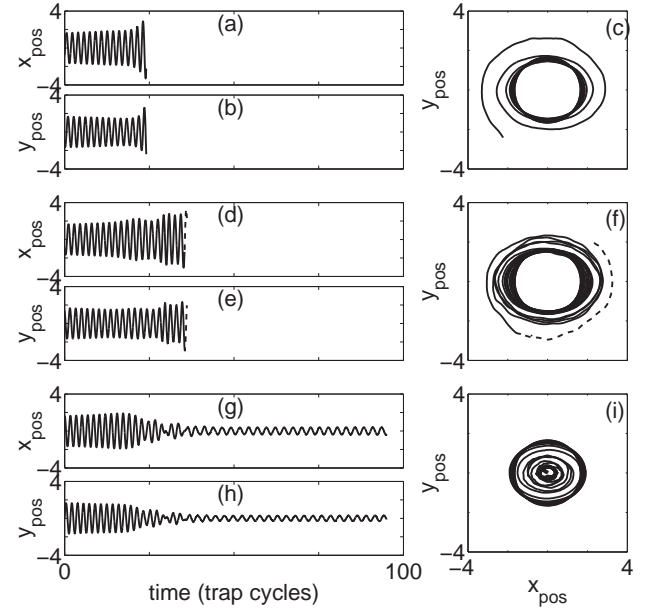


FIG. 11: Breaking of axial symmetry for triangular vortex array for turn-on time of 20 trap cycles for eccentricity parameter $\epsilon = 0.25$ showing (a) x displacement of vortex 1, (b) y displacement of vortex 1, (c) trajectory of vortex 1, (d) x displacement of vortex 2, (e) y displacement of vortex 2, (f) trajectory of vortex 2, and (g) x displacement of vortex 3, (h) y displacement of vortex 3, and (i) trajectory of vortex 3. All positions are in units of the harmonic oscillator length r_0 .

Gross-Pitaevskii equation [32].

Similar simulations were performed for the triangular vortex array with lattice parameter $a = 1.65\sqrt{3}$, where the trapping potential is initially axially symmetric, and the eccentricity is ramped up to $\epsilon = .25$ and $\epsilon = .1$ over a period of 20 trap cycles.

The angular momentum calculated using Eq. (57) is plotted in Fig. 9 I(a) for the case of $\epsilon = 0.25$ and in Fig. 9 II(a) for the case of $\epsilon = 0.1$. Figures 9I(b), and 9II(b) show the respective changes in the thermal and condensate populations and reveal increases in thermal population as each successive vortex spirals outward and finally decays, again in accordance with decay of the vortex into excitations when it reaches the condensate boundary [30]. The simulated absorption images for $\epsilon = .25$ are shown in Figs. 10(a)-10(t), and the vortex trajectories in Figs. 11(a)-11(i). We note from the trajectory of vortex 3, shown in Figs. 11(g) and 11(h), the decrease in the precessional frequency following the departure of a vortex, in agreement with the time-independent predictions for vortex arrays shown in Figs. 3(a) and 3(b), which show the dependence of the precessional frequencies of the vortex array on the lattice parameter for the cases of three vortices (our initial configuration), and of two vortices, and also with Figs. 1(a) and (b) which give the time-independent predicted precessional frequencies for the triangular vortex array at various temperatures and values of lattice parameter. The prediction here is $\Omega \sim .6\omega_r$ for lattice parameter $a \sim 2\sqrt{3} = 3.46$ and is in good agreement with the measured time-dependent value [see Figs. 11(a) and 11(b) for x_{pos} versus T and y_{pos} versus T and the time-independent predictions in Figs. 1(a) and (b)]. We also see good agreement with the measured value of the precessional frequencies of a single vortex (after the other two vortices have left the condensate) indicated in Figs. 11(g) and 11(h), and the time-independent predictions given in Figs. 1(c) and 1(d) in Ref. [15]. We note that Figs. 10 and 11, which show the vortex decay in the case $\epsilon = .25$, are consistent indicating a decay time of ~ 24 trap cycles for the first vortex and a decay time of ~ 38 trap cycles for the second. This is also consistent with Fig. 9I which shows sudden changes in the thermal population at these times, and a steady decrease in L_z with slight drops accompanying the decay of each vortex. We also note a sudden change in the thermal population after ~ 30 trap cycles. This accompanies the complex precessional motion of the third vortex at ~ 30 trap cycles as shown in Figs. 11(g) and 11(h) due to the interaction between the vortices. The lifetimes of the vortices in the case of the triangular vortex for $\epsilon = .25$ vary considerably - the first vortex to leave the condensate has a lifetime of between ~ 20 and ~ 25 trap cycles, while the second has a lifetime varying between ~ 25 and ~ 38 depending on the scenario. In all cases

the loss of a vortex is characterized by a slight drop in L_z and sudden increases in the thermal population with a corresponding drop in the condensate population (see Fig. 9). The departure of the vortices is also marked by the trajectories of the vortices shown in Figs. 11(a)-11(f) where we see the end of the vortex tracks. The lifetime of the remaining vortex can be inferred from Fig. 9 I(a) only by extrapolation and is of the order of 300-400 trap cycles [since the residual angular momentum (i.e. the angular momentum at the time that only a single vortex remains) is higher than in the single vortex case]. In the case of the triangular vortex array for $\epsilon = 0.1$, the lifetime of the first vortex is of the same order ($\sim 25 \rightarrow 30$ trap cycles), but the lifetimes for the second and third vortices are considerably longer, with the second vortex having an extrapolated lifetime of ~ 400 trap cycles [see Fig. 9 II(a)]. It is impossible to ascertain the lifetime of the remaining vortex from the simulations, but it is probably of the order of a few thousand trap cycles that is impractical to simulate with the facilities available.

VII. SUMMARY

We have developed a novel method utilizing the continuity equation for the condensate density to make predictions of the precessional frequency of single off-axis vortices, and of vortex arrays in Bose-Einstein condensates (BECs) at finite temperature. We also presented an orthogonalized Hartree-Fock-Bogoliubov (HFB) formalism for which a zero-energy eigenvalue exists, in contrast to the standard HFB theory. We solved the continuity equation for the condensate density and the time-independent orthogonalized HFB equations self-consistently in the frame rotating at the precessional frequency. Thus we were able to find stationary solutions for quasi-two-dimensional rotating systems in the corotating frame. We compared these results with time-dependent predictions where we simulated stirring of the condensate, finding good agreement with the predicted precessional frequencies. These results are completely consistent with GPE simulations, and are in qualitative agreement with the projected Gross-Pitaevskii simulations and with the areal density law. We also verified that angular momentum is conserved in the quasi-two-dimensional system for an axially symmetric trapping potential and that breaking this symmetry leads to the loss of angular momentum and hence, to the decay of vortices.

This work was funded through the New Economy Research Fund contract NERF-UOOX0703: Quantum Technologies.

[1] A. L. Fetter, Rev. Mod. Phys., **81**, 647 (2009).

[2] D. A. W. Hutchinson, K. Burnett, R. J. Dodd, S. A.

- Morgan, M. Rusch, E. Zaremba, N. P. Proukakis, M. Edwards, and C. W. Clark, *J. Phys. B: At. Mol. Opt. Phys.* **33**, 3825 (2000).
- [3] D. A. W. Hutchinson, E. Zaremba, and A. Griffin, *Phys. Rev. Lett.* **78**, 1842 (1997).
- [4] B. G. Wild, P. B. Blakie, and D. A. W. Hutchinson, *Phys. Rev. A* **73**, 023604 (2006).
- [5] A. Griffin, *Phys. Rev. B* **53**, 9341 (1996).
- [6] I. Coddington, P. C. Haljan, P. Engels, V. Schweikhard, S. Tung, and E. A. Cornell, *Phys. Rev. A* **70**, 063607 (2004).
- [7] D. E. Sheehy and L. Radzihovsky, *Phys. Rev. A* **70**, 051602(R) (2004).
- [8] S. Tung, V. Schweikhard, and E. A. Cornell, *Phys. Rev. Lett.* **97**, 240402 (2006).
- [9] H. Buljan, M. Segev and A. Vardi, *Phys. Rev. Lett.* **95**, 180401 (2005) ; T. Ernst and J. Brand, *Phys. Rev. A* **81**, 033614 (2010).
- [10] S. Wuster, J. J. Hope, and C. M. Savage, *Phys. Rev. A* **71**, 033604 (2005) ; S. Wuster, B. J. Dkabrowska-Wüster, S. M. Scott, J. D. Close and C. M. Savage, *Phys. Rev. A* **77**, 023619 (2008) ; Milstein J. N., Menotti C., and Holland M. J., *New J. Phys.* **5**, 52 (2003).
- [11] Y. Castin and R. Dum, *Rhys. Rev. A* **57**, 3008 (1998).
- [12] This result applies for any linear differential operator $\hat{\mathbf{L}}$, where $\hat{\mathbf{L}} = i\hbar(\mathbf{r} \times \nabla)$ for angular momentum and $\hat{\mathbf{L}} = i\hbar\nabla$ for linear momentum.
- [13] N. M. Hugenholtz and D. Pine, *Phys. Rev.* **116**, 489 (1959).
- [14] D. S. Petrov, M. Holzmann, and G. V. Shlyapnikov, *Phys. Rev. Lett.* **84**, 2551 (2000).
- [15] B. G. Wild and D. A. W. Hutchinson, *Phys. Rev. A* **80**, 035603 (2009).
- [16] H. M. Nilsen, G. Baym, and C. J. Pethick, *Proc. Natl. Acad. Sci. USA*, **103**, 7978 (2006).
- [17] D. M. Jezek and H. M. Cataldo, *Phys. Rev. A* **77**, 043602 (2008).
- [18] M. Guilleumas and R. Graham, *Phys. Rev. A* **64**, 033607 (2001).
- [19] N. Papanicolaou, S. Komineas, and N. R. Cooper, *Phys. Rev. A* **72**, 053609 (2005).
- [20] The simulated absorption images shown are logarithmic plots given by $n_{plot} = \log(n/n_{max})$, where n refers to the specific density to be plotted and n_{max} is the overall maximum density of the BEC (i.e., the maximum of sum of the condensate and non-condensate densities).
- [21] It should be noted that in all cases the precessional frequency of the vortices nucleated in the stirring is distinct from the rotational frequency of the stirrer itself - see for example, Fig. 5 which shows clearly that these precessional frequencies are uncorrelated with the stirring frequency $\Omega_{stir} = 0.5\omega_r$.
- [22] B. M. Caradoc-Davies, R. J. Ballagh and K. Burnett, *Phys. Rev. Lett.* **83**, 895 (1999).
- [23] F. Chevy, K. W. Madison, and J. Dalibard, *Phys. Rev. Lett.* **85**, 2223 (2000).
- [24] C. Raman, M. Köhl, R. Onofrio, D. S. Durfee, C.E. Kulewicz, Z. Hadzibabic, and W. Ketterle, *Phys. Rev. Lett.* **83**, 2502 (1999).
- [25] R. Onofrio, C. Raman, J. M. Vogels, J. R. Abo-Shaeer, A. P. Chikkatur, and W. Ketterle, *Phys. Rev. Lett.* **85**, 2228 (2000).
- [26] P. Engels and C. Atherton, *Phys. Rev. Lett.* **99**, 160405 (2007).
- [27] B. Jackson, J. F. McCann, and C. S. Adams, *Phys. Rev. A* **61**, 051603 (2000).
- [28] Noether E., *Nachr. D. König. Gesellsch. D. Wiss. Zu Göttingen, Math-Phys. Klasse* **2** 235-257 (1918) ; M. A. Peskin and D. V. Schroeder, *An Introduction to Quantum Field Theory*, (Addison-Wesley, Reading, MA, 1995).
- [29] O. N. Zhuravlev, A. E. Muryshev, and P. O. Fedichev, *Phys. Rev. A* **64**, 053601 (2001).
- [30] P. O. Fedichev and G. V. Shlyapnikov, *Phys. Rev. A* **60**, R1779 (1999).
- [31] This is a well-known property of solutions of the GPE [18, 19], provided one is away from the lowest-Landau-Level limit. It is interesting to note that this behavior persists at finite temperature in the HFB solutions.
- [32] T. M. Wright, A. S. Bradley, and R. J. Ballagh, *Phys. Rev. A* **81**, 013610 (2010).